Acta Pharmaceutica Sinica B 2021;11(6):1686−1695

Chinese Pharmaceutical Association
Institute of Materia Medica, Chinese Academy of Medical Sciences

Acta Pharmaceutica Sinica B

www.elsevier.com/locate/apsb
www.sciencedirect.com

SHORT COMMUNICATION

Development of a highly-specific ^{18}F-labeled irreversible positron emission tomography tracer for monoacylglycerol lipase mapping

Zhen Chen[a,†], Wakana Mori[b,†], Jian Rong[a], Michael A. Schafroth[c], Tuo Shao[a], Richard S. Van[d], Daisuke Ogasawara[c], Tomoteru Yamasaki[b], Atsuto Hiraishi[b], Akiko Hatori[b], Jiahui Chen[a], Yiding Zhang[b], Kuan Hu[b], Masayuki Fujinaga[b], Jiyun Sun[a], Qingzhen Yu[a], Thomas L. Collier[a], Yihan Shao[d], Benjamin F. Cravatt[c], Lee Josephson[a], Ming-Rong Zhang[b,*], Steven H. Liang[a,*]

[a]*Division of Nuclear Medicine and Molecular Imaging, Massachusetts General Hospital & Department of Radiology, Harvard Medical School, Boston, MA 02114, USA*
[b]*Department of Advanced Nuclear Medicine Sciences, National Institute of Radiological Sciences, National Institutes for Quantum and Radiological Science and Technology, Chiba 263-8555, Japan*
[c]*The Skaggs Institute for Chemical Biology and Department of Chemical Physiology, The Scripps Research Institute, La Jolla, CA 92037, USA*
[d]*Department of Chemistry and Biochemistry, University of Oklahoma, Norman, OK 73019, USA*

Received 15 October 2020; received in revised form 18 December 2020; accepted 25 January 2021

KEY WORDS

Monoacylglycerol lipase (MAGL);
Central nervous system (CNS);
2-Arachidonylglycerol (2-AG);

Abstract As a serine hydrolase, monoacylglycerol lipase (MAGL) is principally responsible for the metabolism of 2-arachidonoylglycerol (2-AG) in the central nervous system (CNS), leading to the formation of arachidonic acid (AA). Dysfunction of MAGL has been associated with multiple CNS disorders and symptoms, including neuroinflammation, cognitive impairment, epileptogenesis, nociception and neurodegenerative diseases. Inhibition of MAGL provides a promising therapeutic direction for the treatment of these conditions, and a MAGL positron emission tomography (PET) probe would greatly facilitate preclinical and clinical development of MAGL inhibitors. Herein, we design and synthesize a small

*Corresponding authors. Tel.: +81 433 823 709, fax: +81 43 206 3261 (Ming-Rong Zhang); Tel.: +1 617 726 6107, fax: +1 617 726 6165 (Steven H. Liang).

E-mail addresses: zhang.ming-rong@qst.go.jp (Ming-Rong Zhang), liang.steven@mgh.harvard.edu (Steven H. Liang).

[†]These authors made equal contributions to this work.

Peer review under responsibility of Chinese Pharmaceutical Association and Institute of Materia Medica, Chinese Academy of Medical Sciences.

https://doi.org/10.1016/j.apsb.2021.01.021

2211-3835 © 2021 Chinese Pharmaceutical Association and Institute of Materia Medica, Chinese Academy of Medical Sciences. Production and hosting by Elsevier B.V. This is an open access article under the CC BY-NC-ND license (http://creativecommons.org/licenses/by-nc-nd/4.0/).

Arachidonic acid (AA);
Positron emission tomography (PET);
Fluorine-18

library of fluoropyridyl-containing MAGL inhibitor candidates. Pharmacological evaluation of these candidates by activity-based protein profiling identified **14** as a lead compound, which was then radiolabeled with fluorine-18 *via* a facile S_NAr reaction to form 2-[^{18}F]fluoropyridine scaffold. Good blood−brain barrier permeability and high *in vivo* specific binding was demonstrated for radioligand [^{18}F]**14** (also named as [^{18}F]MAGL-1902). This work may serve as a roadmap for clinical translation and further design of potent ^{18}F-labeled MAGL PET tracers.

© 2021 Chinese Pharmaceutical Association and Institute of Materia Medica, Chinese Academy of Medical Sciences. Production and hosting by Elsevier B.V. This is an open access article under the CC BY-NC-ND license (http://creativecommons.org/licenses/by-nc-nd/4.0/).

1. Introduction

As a serine hydrolase, monoacylglycerol lipase (MAGL) exerts a vital role in the endocannabinoid and eicosanoid signalling systems[1−5]. MAGL is widespreadly distributed in the body with particularly high expression in the brain. In the central nervous system (CNS), MAGL catalyses the metabolism of the endocannabinoid 2-arachidonylglycerol (2-AG) to arachidonic acid (AA), approximately constituting 50% AA production, which not only serves as a proinflammatory eicosanoid precursor, but also constitutes inflammatory signals[6−10]. In this case, simultaneous regulation of both endocannabinoid and eicosanoid system constitutes the dual-function of MAGL in the CNS. Recent studies have indicated that dysfunction of MAGL is associated with multiple disorders such as neuroinflammation, cognitive impairment, epileptogenesis, nociception, neurodegenerative diseases, and cancer pathogenesis[11−23]. Inhibition of MAGL not only reduces the production of pro-inflammatory eicosanoids, but also increases 2-AG signaling, thereby providing a promising therapeutic direction for the treatment of the disorders mentioned above. As such, the development of MAGL inhibitors with high affinity and selectivity has caught considerable interest in the field of medicinal chemistry and drug discovery[24−35].

Complementary to routine clinical diagnostic application, positron emission tomography (PET) is a well-characterized noninvasive nuclear imaging tool, which has emerged to be invaluable for target engagement and phase 0 studies in the discovery of CNS drugs[36−38]. Our interest focuses on the discovery of highly MAGL-specific (PET) tracers to enable preclinical and clinical drug development. A MAGL PET tracer would not only allow a deep understanding of biology *in vivo* such as target expression/distribution and relationship with multiple diseases, but also enable a facile clinical translation of MAGL inhibitors. So far, our group[39−42] and others[43−46] have reported several first-in-class ^{11}C-labeled MAGL PET probes with favorable brain permeability and target specificity, such as [^{11}C]SAR127303, [^{11}C]MA-PB-1, [^{11}C]MAGL-0519, [^{11}C]MAGL-2-11 and [^{11}C]PF-06809247. However, the short half-life of carbon-11 ($t_{1/2}$ = 20.4 min) requires on site tracer production, and their utilization is restricted to imaging facilities equipped with a cyclotron. On the other hand, the relatively longer half-life of fluorine-18 ($t_{1/2}$ = 109.7 min) allows for multistep synthesis, extended acquisition time, and transportation over a long distance, thus enabling its off-site use, and has demonstrated great commercialization value. Furthermore, relatively-slow radioactive decay and short positron range of fluorine-18 favorably improves the resolution and counting statistics of PET images. So far, the discovery of ^{18}F-labeled MAGL PET probes is still in its infancy. Only recently, during the preparation of this manuscript, [^{18}F]T-401[47] was developed as an ^{18}F-labeled reversible MAGL PET tracer by Koike and coworkers, whereas [^{18}F]PF06795071[48] was disclosed by our group as an ^{18}F-labeled irreversible MAGL PET probe. By taking advantage of the unique azabicyclo[3.1.0]hexane scaffold, herein we designed and synthesized a focused library of fluoropyridyl-containing MAGL inhibitor candidates (**14**−**17**, Fig. 1). Our hypothesis was that, the incorporation of a fluoropyridyl moiety in **14**−**17** (particularly for 2-fluoropyridyl) instead of the phenyl group in [^{18}F]PF06795071 may facilitate S_NAr labeling with fluorine-18 and decrease the lipophilicity of candidate ligands, thereafter further improving target binding specificity. In this work, our preliminary pharmacological screening and molecular docking studies of these candidates identified **14** as a lead compound. Radiolabeling of **14** with fluorine-18 was achieved *via* a facile S_NAr reaction. MAGL PET ligand [^{18}F]**14** (also named as [^{18}F]MAGL-1902) exhibited excellent brain permeability, high *in vivo* specific binding, and heterogeneous radioactivity accumulation in various brain regions, which was consistent with MAGL expression profile in the brain. This work may serve as a roadmap for PET imaging translation in higher species and guideline for further design of potent ^{18}F-labeled MAGL PET tracers.

2. Results and discussion

2.1. Chemical synthesis

To synthesize irreversible MAGL inhibitors **14**−**17** containing 3-azabicyclo[3.1.0]hexane core unit, we took advantage of a general strategy shown in Scheme 1 with *tert*-butyloxycarbonyl (Boc)-protected 3-azabicyclo[3.1.0]hexane-6-carboxylic acid **1** as the starting material. Briefly, the coupling of **1** with *N*,*O*-dimethylhydroxylamine hydrogen chloride (NHMeOMe·HCl) occurred smoothly to deliver the Weinreb amide **2**. Subsequent Grignard addition converted **2** to the corresponding ketone **3** in 99% yield over two steps. Ketone **3** was then transformed into pyrazole **5** *via* enamine formation and cyclization with hydrazine in 97% total yield. Copper-mediated cross-coupling reaction of pyridyl boronic acid or direct nucleophilic S_NAr substitution of 2-fluoropyridine derivatives with **5** provided compounds **6**−**9** in 8%−52% yield. TFA-triggered removal of the Boc group in **6**−**9** followed by coupling with an activated carbonate *in situ* generated from (*R*)-1,1,1-trifluoro-3-(4-methoxybenzyloxy)propan-2-ol readily proceeded to provide carbamates **10**−**13** in moderate yields

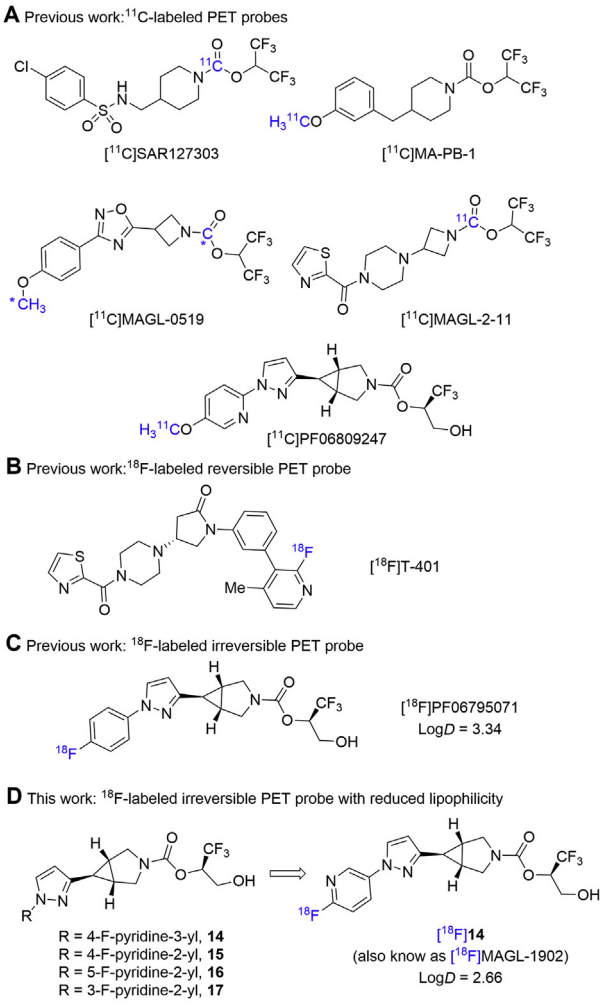

Figure 1 Representative PET probes for brain MAGL imaging.

(26%−41%). Ultimately, the desired MAGL inhibitors **14**−**17** were obtained in a highly efficient manner by deprotection of *p*-methoxybenzyl (PMB) group.

2.2. *Molecular docking studies*

To investigate possible molecular interaction of candidate inhibitors **14**−**17** with MAGL, a "pre-covalent" MAGL−inhibitor complex was constructed by use of molecular docking study. The published MAGL crystal structure (PDB ID: 3PE6)[42,49] was used as the model, and compounds **14**−**17** were then docked into this model by Autodock Vina in a pre-covalent state. As depicted in Fig. 2, all these candidate inhibitors exhibited good interaction with the binding pocket of MAGL and their leaving group oriented towards the Ser122-His269-Asp239 catalytic triad of MAGL, which is a crucial functional unit for the catabolism of 2-AG. In these binding poses, the carbonyl oxygen of candidates **14**−**17** resided close to the residues of Ser122, which possibly formed H-bonding interactions. These results suggested great promise of compounds **14**−**17** to decrease the likelihood of 2-AG to approach the MAGL binding site, thereby being good MAGL inhibitors.

2.3. *Pharmacology*

To probe the potency and selectivity, compounds **14**−**17** were evaluated *in vitro* in mouse brain lysates by activity-based protein profiling (ABPP) with the serine hydrolase directed probe FP-rhodamine[50]. As shown in Fig. 3A, compounds **14**−**16** demonstrated excellent inhibitory activity towards MAGL with single-digit nanomolar IC_{50} values (8.5 nmol/L for **14**, 7.5 nmol/L for **15** and 7.1 nmol/L for **16**). Considering the unique 2-fluoropyridine scaffold in **14**, which enables facile synthesis of the precursor and radiolabeling with fluorine-18, we prioritized this probe for further pharmacological evaluation. As such, the selectivity of compound **14** for inhibition of MAGL over other serine hydrolases, *e.g.*, FAAH, ABHD6, ABHD12 and KIAA1363, was determined by ABPP in mouse brain lysates. In these experiments an excellent selectivity profile was demonstrated with no significant inhibition of serine hydrolase activity of these off-targets (Fig. 3B). To evaluate the reversibility of inhibition, a time-dependent ABPP study was carried out with compound **14** and a known reversible MAGL inhibitor, FEPAD[50], which served as a positive control (Fig. 3C). In this assay, MAGL activity recovered rapidly over time in FEPAD-treated samples, whereas MAGL activity only slowly increased in compound **14**-treated samples, indicating irreversible binding. Furthermore, no direct agonism or antagonism was found for compound **14** with the cannabinoid receptors CB_1 and CB_2 (Fig. 3D−G). An off-target pharmacological screening in major CNS targets, including common GPCRs, enzymes, ion channels and transporters was further carried out for compound **14** at a testing concentration of 10 μmol/L. As illustrated in Supporting Information Fig. S2A, only norepinephrine transporter (NET) was identified with greater than 50% target activity at 10 μmol/L of compound **14**, and a follow-up NET binding assay using [^{3}H] nisoxetine showed the K_i value of **14** to be 4.08 μmol/L (Fig. S2B), indicating more than 400-fold selectivity towards MAGL among other CNS targets tested.

2.4. *Radiochemistry*

With promising pharmacology results, we commenced with the labeling of compound **14** with fluorine-18. The synthesis of bromopyridine precursor **19** was obtained as per the general strategy depicted in Scheme 2. Beginning with pyrazole derivative **5**, 2-bromopyridyl moiety was successfully incorporated *via* a copper-promoted cross-coupling reaction with (6-bromopyridin-3-yl)boronic acid. Deprotection of the Boc group was achieved with TFA, and the corresponding amine intermediate readily underwent alkoxyl-carbonylation reaction with (*R*)-1,1,1-trifluoro-3-(4-methoxybenzyloxy)propan-2-ol and 1,1′-[carbonylbis(oxy)]dipyrrolidine-2,5-dione, thus providing precursor **19** in 54% yield over 2 steps.

With the precursor **19** in hand, we performed its radiolabeling with fluorine-18 to synthesize MAGL PET tracer [^{18}F]**14**. As illustrated in Scheme 3A, S_NAr reaction of **19** with fluorine-18 was achieved by use of K_2CO_3/K222 (0.53 mg/9.4 mg) in DMSO at 150 °C for 10 min (entry 1). Increase of the amount of K_2CO_3 or use of other base such as tetraethylammonium bicarbonate (TEAB) failed to improve this reaction (entries 2 and 3). Complete deprotection of the PMB group was achieved by use of 6 mol/L HCl at 100 °C for 4 min, thus providing an access to radioligand [^{18}F]**14**.

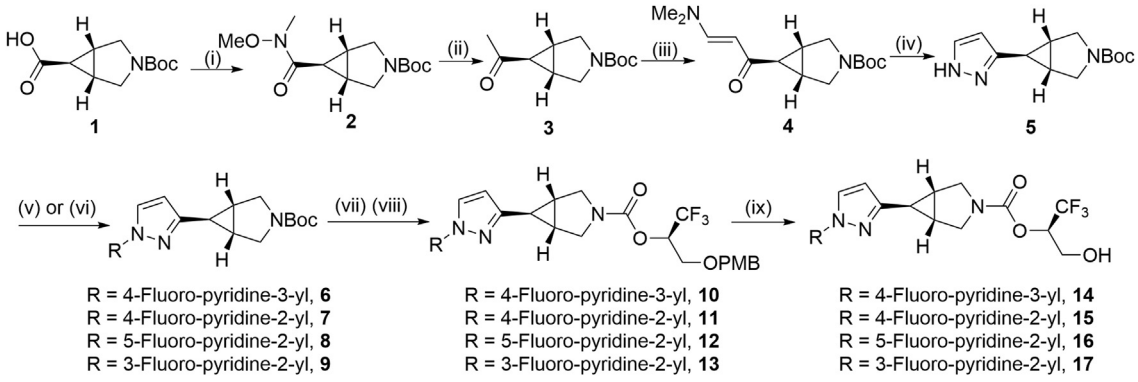

Scheme 1 Synthesis of irreversible MAGL inhibitors **14**−**17**. Conditions: (i) NHMeOMe·HCl, EDC·HCl, DIPEA, HOBT, CH_2Cl_2, rt, 2 h; (ii) MeMgBr, THF, rt, 1 h; 99% yield over 2 steps; (iii) DMF−DMA, DMF, 110 °C, 16 h; (iv) NH_2NH_2, EtOH, 80 °C, 16 h; 97% yield over 2 steps; (v) (6-fluoropyridin-3-yl)boronic acid, pyridine, $Cu(OAc)_2$, 4 Å molecular sieves, CH_2Cl_2, 30 °C, 30 h; 8% yield for **6**; (vi) 2,4-difluoropyridine (for **7**), 2,5-difluoropyridine (for **8**) or 2,3-difluoropyridine (for **9**), Cs_2CO_3, DMF, 120 °C, 24 h; 51% yield for **7**; 48% yield for **8**; 52% yield for **9**; (vii) TFA, rt, 1 h; (viii) Et_3N, 1,1′-[carbonylbis(oxy)]dipyrrolidine-2,5-dione, (*R*)-1,1,1-trifluoro-3-(4-methoxybenzyloxy)propan-2-ol, CH_2Cl_2, 30 °C, 30 h; 26% yield for **10**; 41% yield for **11**;31% yield for **12**; 33% yield for **13**; (ix) TFA, CH_2Cl_2, rt, 4 h; 96% yield for **14**; 67% yield for **15**; 74% yield for **16**; 92% yield for **17**; NHMeOMe·HCl=*N*,*O*-dimethylhydroxylamine hydrogen chloride; EDC·HCl=*N*-(3-dimethylaminopropyl)-*N*′-ethylcarbodiimide hydrochloride; DIPEA=*N*,*N*-diisopropylethylamine; HOBT = 1-hydroxybenzotriazole hydrate; Et_3N = triethylamine; DMF = *N*,*N*-dimethylformamide; TFA = trifluoroacetic acid; PMB = *p*-methoxybenzyl.

This protocol features several merits such as reasonable radiochemical yield (11% RCY, decay-corrected), good molar activity (up to 210 GBq/μmol) and high radiochemical purity (>99%) at end of synthesis. Of note, no radiolysis was observed up to 5 h in ethanol-containing saline (5%), which implicated excellent formulation stability for radioligand [^{18}F]**14** (Scheme 3B). In addition, in the discovery of CNS PET tracers, favorable physicochemical property is crucial to increase the likelihood of the passive blood−brain barrier (BBB) permeability and decrease the risk of non-specific binding. In this case, the lipophilicity of ligand [^{18}F]**14** ($\log D = 2.66 \pm 0.01, n = 3$) was determined by the 'shake flask method', also well-characterized as liquid−liquid partition between *n*-octanol and PBS[51], the value of which was aligned within the favorable space (1.0−3.5) of PET CNS tracers[52−54].

2.5. *Preliminary PET imaging and whole-body biodistribution studies of [^{18}F]**14***

Radioligand [^{18}F]**14** was then advanced to PET imaging evaluation. Dynamic rat brain PET images were collected under baseline and blocking conditions for 90 min post intravenous administration of [^{18}F]**14** to Sprague−Dawley (SD) rats. Fig. 4 illustrated the co-registration of summed PET images (0−20, 20−50 and 50−90 min) with magnetic resonance imaging (MRI)

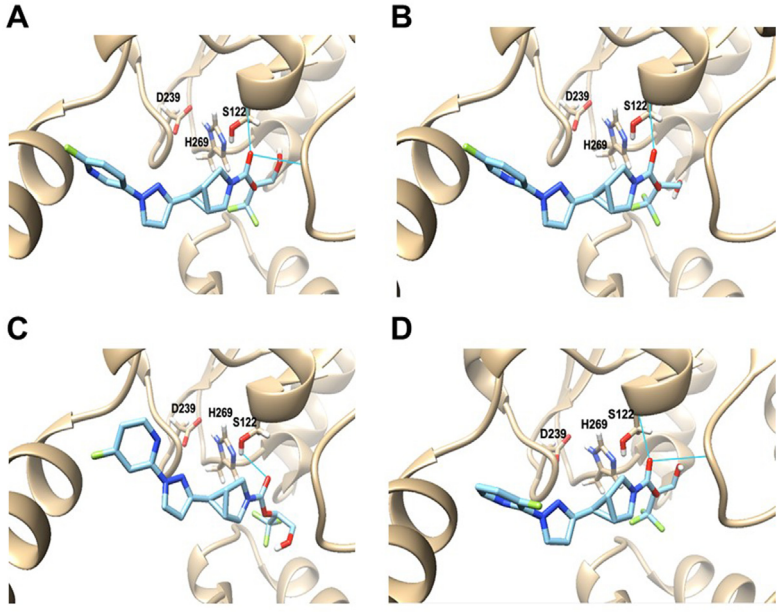

Figure 2 Molecular docking structures of compounds **14** (A), **15** (B) **16** (C) and **17** (D) onto MAGL (pre-covalent docking state). H-bonding interactions between compounds **14**−**17** and MAGL residues were labeled by blue lines. PDB ID: 3PE6.

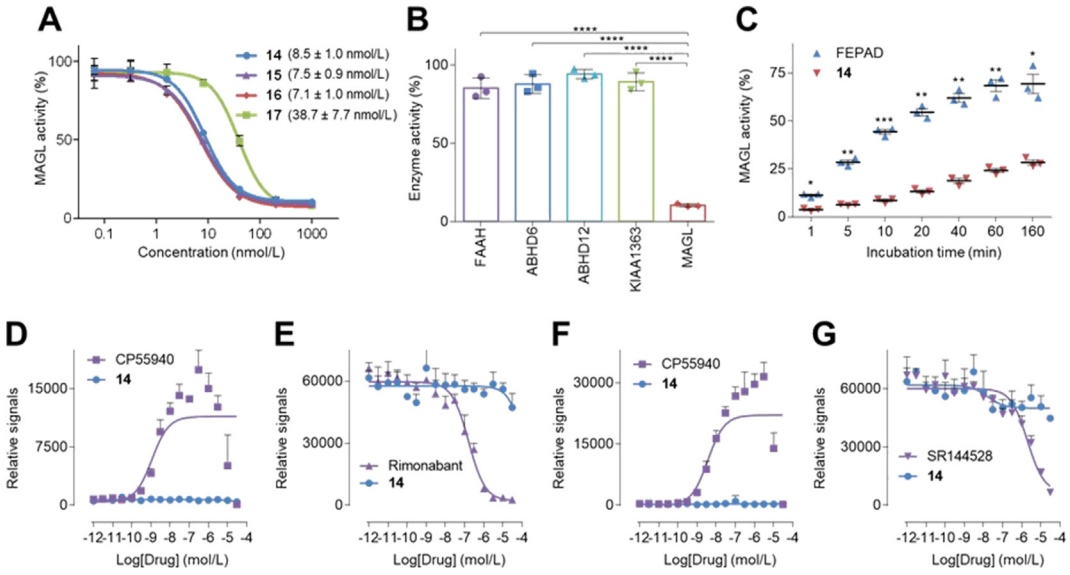

Figure 3 Pharmacological evaluation of compounds **14**–**17**. (A) Concentration–response curves of candidates **14**–**17** for inhibiting mouse brain MAGL activity; (B) Selectivity of **14** at a concentration of 0.2 μmol/L among MAGL and other serine hydrolases, *e.g.*, FAAH, ABHD6, ABHD12 and KIAA1363; (C) Time-dependent ABPP activity of **14** at a concentration of 1 μmol/L with the reversible inhibitor FEPAD (1 μmol/L) as control. (D) CB_1 agonist assay with CP55940 as control; (E) CB_1 antagonist assay with rimonabant as control; (F) CB_2 agonist assay with CP55940 as control; (G) CB_2 antagonist assay with SR144528 as control. All data are indicated as mean ± SD, $n = 3$. A student's two-tailed *t*-test was carried out for statistical analysis and asterisks referred to the statistical significance: $^*P < 0.05$, $^{**}P \leq 0.01$, $^{***}P \leq 0.001$, and $^{****}P \leq 0.0001$.

images as well as the corresponding time–activity curves (TAC). The baseline scan demonstrated good BBB penetration ability for [^{18}F]**14** (Fig. 4A), and the maximum brain uptake was achieved at 1.5 min post tracer injection with the standard uptake value (SUV) of 1.3, as indicated by the whole-brain TAC (Fig. 4D). In addition, radioligand [^{18}F]**14** also implicated a heterogeneous distribution pattern, and high radioactivity were accumulated in the striatum, hippocampus and cerebral cortex, whereas pons exhibited low radioactivity accumulation. Of note, the slow elimination of [^{18}F]**14** from rat brain over time is possibly attributed to a slow hydrolysis of the inhibitor–MAGL adduct, which was also observed in the ABPP studies. Following a 30 min pretreatment with KML29 under a dose of 0.3 mg/kg, a well-characterized MAGL inhibitor, the uptake of [^{18}F]**14** in various brain regions all reduced significantly, thereby leading to the abolishment of heterogeneous distribution pattern in baseline scans (Supporting Information Fig. S3). Of note, increasing the dose of KML29 to 3 mg/kg could further enhanced this radioactivity reduction in all brain regions with a robust attenuation of the whole-brain uptake by 57% as per the area under the curve (AUC), which suggested high *in vivo* binding specificity and a dose-dependent blocking of the binding of [^{18}F]**14** in rat brains (Fig. 4B, E and Fig. S3). To further assess the *in vivo* specificity of [^{18}F]**14**, we then carried out another pretreatment experiment with PF06795071 (3 mg/kg), a potent MAGL inhibitor disclosed by Pfizer[31]. As expected, a robust blocking was seen in the rat brain images and the corresponding TAC (45% reduction of whole-brain uptake as per AUC, Fig. 4C and E). Motivated by these promising results, we then conducted whole-body biodistribution studies aiming to further examine *in vivo* uptake and washout of [^{18}F]**14** in peripheral organs of rodents. As illustrated in Fig. 5 and Supporting Information Table S1, CD-1 mice were used as objects and four time points (5, 15, 30 and 60 min) was selected post injection of [^{18}F]**14**. Radioactivity was robustly accumulated in multiple peripheral organs of CD-1 mice, such as the heart, liver kidneys, lungs, small intestine, and pancreas with levels of higher than 5% ID/g (injected dose per gram of wet tissue) at 5 min post tracer injection. Following initial high uptake, the radioactivity of [^{18}F]**14** in the kidneys and liver slowly washed out, and high radioactivity level was observed in the small intestine at 60 min after injecting [^{18}F]**14**, which implicated a possible hepatobiliary and urinary elimination pathway for [^{18}F]**14**. To further showcase the pharmacokinetic properties of [^{18}F]**14**, we performed whole-body PET imaging studies in mice. As

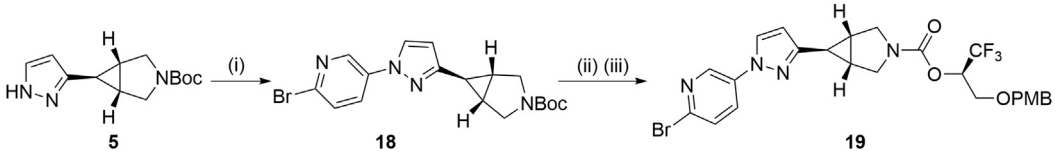

Scheme 2 Synthesis of precursor **19** and its radiolabeling en route to MAGL PET tracer **20** ([^{18}F]**14**). Conditions: (i) (6-bromopyridin-3-yl) boronic acid, $Cu(OAc)_2$, pyridine, 4 Å molecular sieves, CH_2Cl_2, 30 °C, 30 h; 9% yield; (ii) TFA, rt, 1 h; (iii) Et_3N, 1,1′-[carbonylbis(oxy)] dipyrrolidine-2,5-dione, (*R*)-1,1,1-trifluoro-3-(4-methoxybenzyloxy)pro-pan-2-ol, CH_2Cl_2, 30 °C, 30 h; 54% yield over two steps. TFA = trifluoroacetic acid; PMB = *p*-methoxybenzyl.

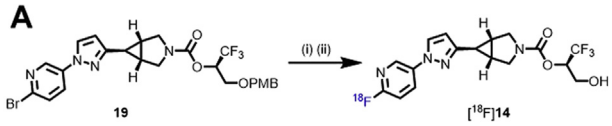

Entry	base	Solvent	Temperature	RCC for step (i)
1	**K_2CO_3 (0.53 mg)**	**DMSO**	**150 °C**	**20% (11%)[a]**
2	K_2CO_3 (2 mg)	DMSO	150 °C	4%
3	TEAB (1 mg)	DMF	100 °C	0%

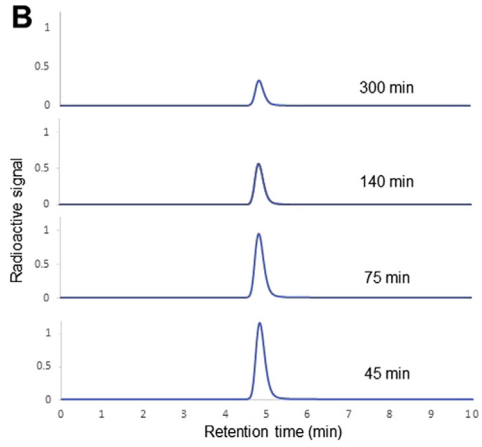

Scheme 3 (A) Radiosynthesis of MAGL PET tracer [^{18}F]**14**. Conditions: (i) $^{18}F^-$, K_2CO_3, K222, DMSO, 150 °C, 10 min; (ii) 6 mol/L HCl, 100 °C, 4 min. [a]The value in parenthesis refers to an average radiochemical yield over two steps (decay-corrected). (B) Stability of tracer [^{18}F]**14** in saline containing 5% of EtOH. RCC = radiochemical conversion.

showed in Supporting Information Fig. S4, initial high radioactivity level was observed in major peripheral organs such as liver, heart, lungs and kidneys, followed by steady wash-out, which is in line with the results from whole-body bio-distribution studies. At 60 min post tracer injection, the radioactivity level reached a relatively steady state in almost all the organs. The relative low uptake of [^{18}F]**14** in brown fat tissues (BAT) was probably caused by anesthesia and the radioactivity in BAT gradually accumulated over 5 min, and no significant elimination was observed, which complies with the irreversible binding profile. To probe the stability of [^{18}F]**14** *in vivo*, we performed a radiometabolic analysis in the brain and plasma homogenate of SD rats. With our previously developed method, we demonstrated that most of the radioactivity in rat brain was bound irreversibly to the brain tissues and the bound radioactivity fraction was determined to be 84% and 75% at 5 and 30 min post tracer injection ($n = 3$), respectively. In the meanwhile, we also investigated the metabolites of unbound radioactivity in rat brains and an average of 78% and 64% of parent radioactivity was observed at 5 and 30 min post tracer injection, respectively ($n = 2$). For radioactivity in plasma, the parent fraction was determined with an average of 70% and 46% of radioactivity at 5 and 30 min post tracer injection, respectively ($n = 2$). These results indicated favorable *in vivo* stability of [^{18}F]**14** in rats.

3. Conclusions

We have successfully designed and synthesized a focused library of fluoropyridyl-containing MAGL inhibitor candidates on the basis of unique azabicyclo[3.1.0]hexane scaffold. The molecular interaction between these candidates and MAGL binding pocket was predicted by molecular docking studies. Pharmacological assessment by ABPP in mouse brain lysates identified **14** as a potent and selective lead compound. The radioligand [^{18}F]**14** (also called [^{18}F]MAGL-1902) was achieved *via* a facile S_NAr reaction on the 2-fluoropyridine scaffold with reasonable radiochemical yield, favorable molar activity and high radiochemical purity. Good BBB permeability, characteristic heterogeneous brain distribution and high *in vivo* binding specificity were demonstrated by PET studies. To further showcase the translation value of this [^{18}F]**14**, comprehensive PET imaging studies in mouse models of MAGL deficiency and higher species with kinetic modeling is necessary in the future work. This work may provide a roadmap and guideline for further design of potent ^{18}F-labeled MAGL PET tracers and translation into higher species, such as nonhuman primates and human subjects.

4. Experimental

4.1. General information

The experimental procedures used in this work were slightly modified from literatures[41,48]. All the chemicals used in the synthesis of MAGL inhibitors and the corresponding precursor were directly acquired from commercial vendors without any purification. Silica gel was used for the purification of synthetic compounds by column chromatography and 0.25 mm silica gel plates were used as indicator for TLC. To obtain the NMR spectra of synthetic compounds, a 300 MHz Bruker spectrometer was used. "ppm" was used to indicate the chemical shifts (δ) and "Hertz" was the unit of coupling constants. The abbreviations of multiplicities for peaks in HNMR and FNMR spectra were described as follows: s (singlet), d (doublet), dd (doublet of doublets), t (triplet), q (quartet), m (multiple), and br (broad signal). For the measurement of mass spectrometer, Agilent 6430 Triple Quad LC/MS was adopted with ESI as the ionization approach. No promiscuity was observed in the assay of PAINS (Pan Assay Interference Compounds) for all candidate compounds **14**–**17** with two in silico filters (http://zinc15.docking.org/patterns/home and http://www.swissadme.ch/index.php)[55]. High purity (≥95%) was also determined for lead compound **14** by a reverse-phase HPLC (Agilent 5 μm, Eclipse plus C18 column (100 mm × 4.6 mm). Unless noted otherwise, molar activity was determined at the end of synthesis. All animal studies were carried out following the ethical rules of Massachusetts General Hospital and National Institute of Radiological Sciences. CD-1 mice (female, 22–24 g, 7 weeks), SD rats (male, 210–230 g, 7 weeks) were feeded *ad libitum* with food and water under a condition of 12 h light/12 h dark cycle.

4.2. Radiosynthesis of [^{18}F]14

[^{18}F]F^- was generated by the $^{18}O(p,n)^{18}F$ reaction performed in the cyclotron using 18 MeV protons and >98% enriched $H_2^{18}O$ (ROTEM Industries, Arava, Israel). An automated synthetic module was used in this work. The [^{18}F]F^- generated from the cyclotron was purified from $H_2^{18}O$ by use of an anion-exchange cartridge (Sep-Pak QMA Plus Light cartridge; Waters). The elution of [^{18}F]F^- from the cartridge was achieved with a solution of K_2CO_3 (0.53 mg) and Kryptofix 222 (9.4 mg) in water (250 μL) and acetonitrile (250 μL). The eluted [^{18}F]F^- solution was then

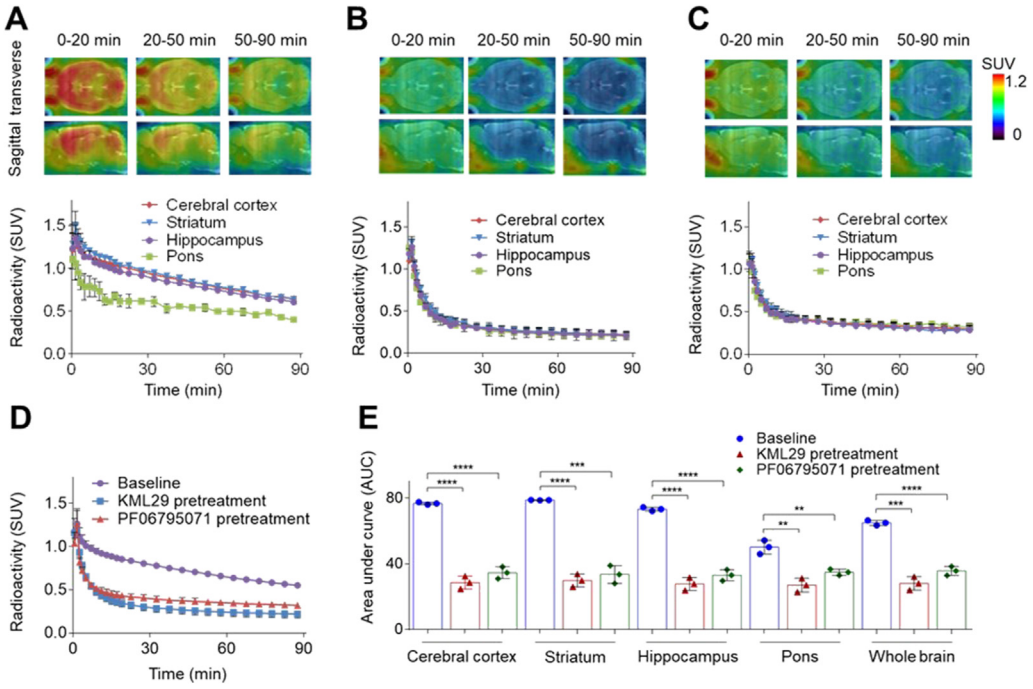

Figure 4 Summed PET images and representative time−activity curves (TACs) of [^{18}F]**14** in rat brains under (A) Baseline conditions; (B) Pretreatment conditions with KML29 (3 mg/kg); (C) Pretreatment conditions with PF06795071 (3 mg/kg). (D) Whole-brain TACs; (E) Area under curves. $^{**}P \leq 0.01$, $^{***}P \leq 0.001$, and $^{***}P \leq 0.0001$.

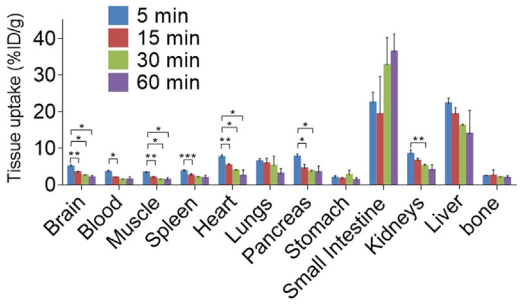

Figure 5 *Ex vivo* whole-body biodistribution studies. The statistical significance was expressed with asterisks: $^{*}P < 0.05$, $^{**}P \leq 0.01$, and $^{***}P \leq 0.001$.

transferred to a reaction vessel and dried at 110 °C with a helium flow. Then a solution of bromopyridine precursor **19** (1.5 mg) in dry-DMSO (300 μL) was added, and the reaction vial containing precursor and dry [^{18}F]F^{-} was heated at 150 °C for 10 min before cooling to 60 °C. Then 6 mol/L HCl (500 μL) was added and heated at 100 °C (4 min) to remove the PMB group. After cooling to room temperature, 6 mol/L NaOH (500 μL) was added and the resulting mixture was purified through a semi-preparative HPLC (CAPCELL PAK C18 UG80, 5 μL, 250 mm × 10 mm) with an eluent of CH_3CN/H_2O (45/55, *v/v*) at a flow rate of 5.0 mL/min. A wavelength of 254 nm was used for the UV monitor. The radioactive [^{18}F]**14** fraction with a retention time of 9.5 min was collected with a flask containing ethanol (300 μL), Tween 80 (75 μL), and 25% ascorbic acid aqueous solution (0.1 mL). The mixture was then concentrated *in vacuo* and redissolved in 3 mL of saline containing 5% ethanol to obtain [^{18}F]**14**. The chemical and radiochemical purity were measured by use of an analytical HPLC (OOF-4454-YO, Gemini 5 μm, 150 mm × 3 mm) with an eluent of CH_3CN/H_2O (40/60, *v/v*) at a flow rate of 1.0 mL/min. The retention time of [^{18}F]**14** was 5.2 min. The decay-corrected radiochemical yield of [^{18}F]**14** was determined to be 11% with good molar activity (up to 210 GBq/mmol) and high radiochemical purity (>99%).

4.3. *Molecular docking studies*

The procedure for molecular docking studies in this work was slightly modified from literature[48]. We first downloaded the crystal structure of soluble human MAGL with a resolution of 1.35 Å (PDB ID: 3PE6). The original ligand was re-docked into the binding site, and its binding pose from Autodock Vina exhibited a good overlapping with the original one. Compounds **14**−**17** were then docked into the aforementioned 3PE6 structure.

4.4. *Activity-based protein profiling (ABPP)*

The procedure of ABPP assay in this work was slightly modified from literatures[41,56]. In brief, 1 mg/mL membrane proteomes from mouse brain were first incubated at 37 °C together with a candidate MAGL inhibitor or DMSO as negative control for 30 min. FP-rhodamine was then added to give a final concentration of 0.5 μmol/L. After incubating at room temperature for another 15 min, 4 × SDS loading buffer was introduced to stop the reaction and the reaction mixture was separated with SDS−PAGE. A ChemiDoc MP system was used to visualize the samples by in-gel fluorescence scanning. For time-dependent studies, the membrane proteomes are preincubated at 37 °C with 1 μmol/L compound **14** for 30 min before incubation with FP-Rh at room temperature for different time (1−160 min) with a final concentration of 0.5 μmol/L. Herein the reversible MAGL inhibitor

FEPAD[50] was choosed as the positive control. Three parallel experiments were carried out and the data was indicated as an average of 3 runs. The intensity of DMSO-treated proteomes was normalized to 100% and the relative intensity of candidate MAGL inhibitors was acquired by comparison.

4.5. CB_1 and CB_2 binding assays

The profiles for CB_1 and CB_2 binding of **14** were obtained following literatures[57,58] and the procedures were described on the Website (https://pdspdb.unc.edu/pdspWeb, assay protocol book). This experiment was supported by the National Institute of Mental Health's Psychoactive Drug Screening Program. In both CB_1 and CB_2 agonist assays, compound CP55940 was adopted as the positive control, while in CB_1 and CB_2 antagonist assays, Rimonabant and SR144528 was adopted as the positive control, respectively. Three to five parallel experiments were carried out and the data was indicated as an average of 3−5 runs.

4.6. Measurement of logD

The procedure for measuring the lipophilicity in this work was slightly modified from literatures[40,41]. In brief, to obtain the log*D* values, [^{18}F]**14**, *n*-octanol (3 mL) and PBS (0.1 mol/L, 3 mL) was mixed in a centrifugal tube, and vortex was performed for 3 min followed by 5 min's centrifuge (∼14,000 rpm). Before use of PBS and *n*-octanol, pre-saturation with each other needs to be performed. PBS (500 μL) and *n*-octanol (50 μL) were then aliquoted and weighted. An autogamma counter (Cobra Model 5002/5003) was used to determine the radioactivity. The log*D* was calculated with Eq. (1):

$$\text{Log}D = \text{Log}[(\text{radioactivity}_{n\text{-octanol}}/\text{weight}_{n\text{-octanol}})/(\text{radioactivity}_{\text{PBS}}/\text{weight}_{\text{PBS}})] \quad (1)$$

Three parallel experiments were carried out and the data was indicated as an average of 3 runs.

4.7. Small-animal PET imaging studies

The procedure for PET imaging studies in this work was slightly modified from literatures[40,41]. An Inveon PET scanner (Siemens) was used to acquire PET scans and during the scan 1%−2% isoflurane/air (*v*/*v*) was used to keep the Sprague−Dawley rats under anesthesia. Intravenous injection of radioligand [^{18}F]**14** (*ca.* 0.5 mCi/150 μL) was performed by use of a preinstalled catheter and the dynamic PET images were then collected for 90 min in a 3D mode. For blocking experiments, intravenous injection of KML29 (3 mg/kg) or PF06795071 (3 mg/kg) was carried out 30 min before injecting [^{18}F]**14**. As we described previously[40,59,60], ASIPro VW software was used for the reconstruction of the dynamic PET images and the achievement of the volumes of interest, such as the whole brain and various brain regions. The radioactivity was indicated with SUV as Eq. (2):

$$\text{SUV} = (\text{Radioactivity per mL tissue/Injected radioactivity}) \times \text{Body weight} \quad (2)$$

4.8. Ex vivo whole body biodistribution of [^{18}F]**14** in mice

The procedure for biodistribution experiments in this work was slightly modified from literatures[40,41]. In brief, [^{18}F]**14** (20 μCi/100 μL) was intravenously injected *via* the tail vein of CD-1 mice. At different time points (5, 15, 30 and 60 min) after injecting [^{18}F]**14**, the mice were sacrificed and organs of interest were collected and weighted. An autogamma counter (Cobra Model 5002/5003) was used to determine the radioactivity in each organ. All experiments were repeated 4 times and the data was an average of 4 runs indicated as the percentage of injected dose per gram of wet tissue (%ID/g).

Acknowledgments

We thank Professor Thomas J. Brady (Nuclear Medicine and Molecular Imaging, Radiology, MGH and Harvard Medical School, USA) for helpful discussion. We also thank the National Institute of Mental Health's Psychoactive Drug Screening Program (NIMH PDSP; directed by Bryan L. Roth at the University of North Carolina at Chapel Hill and Jamie Driscoll at NIMH, USA) for *in vitro* screening. We also gratefully acknowledge the financial support from the NIH grants (DA038000 and DA043507 to S. H. L. and DA033760 to B. F. C.) and the Swiss National Science Foundation for a postdoctoral fellowship to Michael A. Schafroth (Grant No. P2EZP3_175137, Switzerland).

Author contributions

All the authors contributed to this manuscript and have approved its final version. Zhen Chen and Steven H. Liang designed the studyand wrote the manuscript. Zhen Chen, Wakana Mori, Jian Rong, Michael A. Schafroth, Tuo Shao, Richard S. Van, Daisuke Ogasawara, Tomoteru Yamasaki, Atsuto Hiraishi, Akiko Hatori, Jiahui Chen, Yiding Zhang, Kuan Hu, Masayuki Fujinaga, Jiyun Sun and Qingzhen Yu performed experiments. Thomas L. Collier, Yihan Shao, Benjamin F. Cravatt and Lee Josephson designed and guided experiments. Ming-Rong Zhang and Steven H. Liang conceived project and wrote the manuscript.

Conflicts of interest

The authors have no conflicts of interest to declare.

Appendix A. Supporting information

Supporting information to this article can be found online at https://doi.org/10.1016/j.apsb.2021.01.021.

References

1. Di Marzo V, Bisogno T, De Petrocellis L. Endocannabinoids and related compounds: walking back and forth between plant natural products and animal physiology. *Chem Biol* 2007;**14**:741−56.
2. Ahn K, McKinney MK, Cravatt BF. Enzymatic pathways that regulate endocannabinoid signaling in the nervous system. *Chem Rev* 2008;**108**:1687−707.
3. Gil-Ordóñez A, Martín-Fontecha M, Ortega-Gutiérrez S, López-Rodríguez ML. Monoacylglycerol lipase (MAGL) as a promising therapeutic target. *Biochem Pharmacol* 2018;**157**:18−32.
4. Grabner GF, Zimmermann R, Schicho R, Taschler U. Monoglyceride lipase as a drug target: at the crossroads of arachidonic acid

metabolism and endocannabinoid signaling. *Pharmacol Ther* 2017; **175**:35−46.
5. Chanda PK, Gao Y, Mark L, Btesh J, Strassle BW, Lu P, et al. Monoacylglycerol lipase activity Is a critical modulator of the tone and integrity of the endocannabinoid system. *Mol Pharmacol* 2010;**78**: 996−1003.
6. Mechoulam R, Ben-Shabat S, Hanus L, Ligumsky M, Kaminski NE, Schatz AR, et al. Identification of an endogenous 2-monoglyceride, present in canine gut, that binds to cannabinoid receptors. *Biochem Pharmacol* 1995;**50**:83−90.
7. Sugiura T, Kondo S, Sukagawa A, Nakane S, Shinoda A, Itoh K, et al. 2-Arachidonoylgylcerol: a possible endogenous cannabinoid receptor ligand in brain. *Biochem Biophys Res Commun* 1995;**215**:89−97.
8. Stella N, Schweitzer P, Piomelli D. A second endogenous cannabinoid that modulates long-term potentiation. *Nature* 1997;**388**:773−8.
9. Piomelli D. The molecular logic of endocannabinoid signalling. *Nat Rev Neurosci* 2003;**4**:873−84.
10. Chevaleyre V, Takahashi KA, Castillo PE. Endocannabinoid-mediated synaptic plasticity in the CNS. *Annu Rev Neurosci* 2006;**29**:37−76.
11. Chiurchiù V, Battistini L, Maccarrone M. Endocannabinoid signalling in innate and adaptive immunity. *Immunology* 2015;**144**:352−64.
12. Long JZ, Li W, Booker L, Burston JJ, Kinsey SG, Schlosburg JE, et al. Selective blockade of 2-arachidonoylglycerol hydrolysis produces cannabinoid behavioral effects. *Nat Chem Biol* 2009;**5**:37−44.
13. Long JZ, Nomura DK, Cravatt BF. Characterization of monoacylglycerol lipase inhibition reveals differences in central and peripheral endocannabinoid metabolism. *Chem Biol* 2009;**16**:744−53.
14. Nomura DK, Long JZ, Niessen S, Hoover HS, Ng SW, Cravatt BF. Monoacylglycerol lipase regulates a fatty acid network that promotes cancer pathogenesis. *Cell* 2010;**140**:49−61.
15. Nomura DK, Lombardi DP, Chang JW, Niessen S, Ward AM, Long JZ, et al. Monoacylglycerol lipase exerts dual control over endocannabinoid and fatty acid pathways to support prostate cancer. *Chem Biol* 2011;**18**:846−56.
16. Nomura DK, Morrison BE, Blankman JL, Long JZ, Kinsey SG, Marcondes MC, et al. Endocannabinoid hydrolysis generates brain prostaglandins that promote neuroinflammation. *Science* 2011;**334**: 809−13.
17. Ye L, Zhang B, Seviour EG, Tao KX, Liu XH, Ling Y, et al. Monoacylglycerol lipase (MAGL) knockdown inhibits tumor cells growth in colorectal cancer. *Cancer Lett* 2011;**307**:6−17.
18. Chen R, Zhang J, Wu Y, Wang D, Feng G, Tang YP. Monoacylglycerol lipase is a therapeutic target for Alzheimer's disease. *Cell Rep* 2012;**2**: 1329−39.
19. Jung K-M, Clapper JR, Fu J, D'Agostino G, Guijarro A, Thongkham D, et al. 2-Arachidonoylglycerol signaling in forebrain regulates systemic energy metabolism. *Cell Metabol* 2012;**15**: 299−310.
20. Cao Z, Mulvihill MM, Mukhopadhyay P, Xu H, Erdélyi K, Hao E, et al. Monoacylglycerol lipase controls endocannabinoid and eicosanoid signaling and hepatic injury in mice. *Gastroenterology* 2013;**144**: 808−17.
21. Costola-de-Souza C, Ribeiro A, Ferraz-de-Paula V, Calefi AS, Aloia TPA, Gimenes-Júnior JA, et al. Monoacylglycerol lipase (MAGL) inhibition attenuates acute lung injury in mice. *PLoS One* 2013;**8**:e77706.
22. Griebel G, Pichat P, Beeske S, Leroy T, Redon N, Jacquet A, et al. Selective blockade of the hydrolysis of the endocannabinoid 2-arachidonoylglycerol impairs learning and memory performance while producing antinociceptive activity in rodents. *Sci Rep* 2015;**5**: 7642.
23. Mulvihill MM, Nomura DK. Therapeutic potential of monoacylglycerol lipase inhibitors. *Life Sci* 2013;**92**:492−7.
24. Long JZ, Jin X, Adibekian A, Li W, Cravatt BF. Characterization of tunable piperidine and piperazine carbamates as inhibitors of endocannabinoid hydrolases. *J Med Chem* 2010;**53**:1830−42.
25. Chang JW, Niphakis MJ, Lum KM, Cognetta AB, Wang C, Matthews ML, et al. Highly selective inhibitors of monoacylglycerol lipase bearing a reactive group that is bioisosteric with endocannabinoid substrates. *Chem Biol* 2012;**19**:579−88.
26. Afzal O, Kumar S, Kumar R, Firoz A, Jaggi M, Bawa S. Docking based virtual screening and molecular dynamics study to identify potential monoacylglycerol lipase inhibitors. *Bioorg Med Chem Lett* 2014;**24**:3986−96.
27. Korhonen J, Kuusisto A, van Bruchem J, Patel JZ, Laitinen T, Navia-Paldanius D, et al. Piperazine and piperidine carboxamides and carbamates as inhibitors of fatty acid amide hydrolase (FAAH) and monoacylglycerol lipase (MAGL). *Bioorg Med Chem* 2014;**22**: 6694−705.
28. Brindisi M, Maramai S, Gemma S, Brogi S, Grillo A, Di Cesare Mannelli L, et al. Development and pharmacological characterization of selective blockers of 2-arachidonoyl glycerol degradation with efficacy in rodent models of multiple sclerosis and pain. *J Med Chem* 2016;**59**:2612−32.
29. Butler CR, Beck EM, Harris A, Huang Z, McAllister LA, Am Ende CW, et al. Azetidine and piperidine carbamates as efficient, covalent inhibitors of monoacylglycerol lipase. *J Med Chem* 2017;**60**: 9860−73.
30. Cisar JS, Weber OD, Clapper JR, Blankman JL, Henry CL, Simon GM, et al. Identification of ABX-1431, a selective inhibitor of monoacylglycerol lipase and clinical candidate for treatment of neurological disorders. *J Med Chem* 2018;**61**:9062−84.
31. McAllister LA, Butler CR, Mente S, O'Neil SV, Fonseca KR, Piro JR, et al. Discovery of trifluoromethyl glycol carbamates as potent and selective covalent monoacylglycerol lipase (MAGL) inhibitors for treatment of neuroinflammation. *J Med Chem* 2018;**61**: 3008−26.
32. Hernández-Torres G, Cipriano M, Hedén E, Björklund E, Canales Á, Zian D, et al. A reversible and selective inhibitor of monoacylglycerol lipase ameliorates multiple sclerosis. *Angew Chem Int Ed* 2014;**53**: 13765−70.
33. Granchi C, Rizzolio F, Palazzolo S, Carmignani S, Macchia M, Saccomanni G, et al. Structural optimization of 4-chlorobenzoylpiperidine derivatives for the development of potent, reversible, and selective monoacylglycerol lipase (MAGL) inhibitors. *J Med Chem* 2016;**59**:10299−314.
34. Aghazadeh Tabrizi M, Baraldi PG, Baraldi S, Ruggiero E, de Stefano L, Rizzolio F, et al. Discovery of 1,5-diphenylpyrazole-3-carboxamide derivatives as potent, reversible, and selective monoacylglycerol lipase (MAGL) inhibitors. *J Med Chem* 2018;**61**:1340−54.
35. Aida J, Fushimi M, Kusumoto T, Sugiyama H, Arimura N, Ikeda S, et al. Design, synthesis, and evaluation of piperazinyl pyrrolidin-2-ones as a novel series of reversible monoacylglycerol lipase inhibitors. *J Med Chem* 2018;**61**:9205−17.
36. Ametamey SM, Honer M, Schubiger PA. Molecular imaging with PET. *Chem Rev* 2008;**108**:1501−16.
37. Willmann JK, van Bruggen N, Dinkelborg LM, Gambhir SS. Molecular imaging in drug development. *Nat Rev Drug Discov* 2008;**7**: 591−607.
38. Miller PW, Long NJ, Vilar R, Gee AD. Synthesis of ^{11}C, ^{18}F, ^{15}O, and ^{13}N radiolabels for positron emission tomography. *Angew Chem Int Ed* 2008;**47**:8998−9033.
39. Wang L, Mori W, Cheng R, Yui J, Rotstein B, Fujinaga M, et al. A novel class of sulfonamido [^{11}C-carbonyl]-labeled carbamates and ureas as radiotracers for monoacylglycerol lipase. *J Nucl Med* 2016; **57**:4.
40. Wang L, Mori W, Cheng R, Yui J, Hatori A, Ma L, et al. Synthesis and preclinical evaluation of sulfonamido-based [^{11}C-carbonyl]-carbamates and ureas for imaging monoacylglycerol lipase. *Theranostics* 2016;**6**:1145−59.
41. Cheng R, Mori W, Ma L, Alhouayek M, Hatori A, Zhang Y, et al. *In vitro* and *in vivo* evaluation of ^{11}C-labeled azetidinecarboxylates for imaging monoacylglycerol lipase by PET imaging studies. *J Med Chem* 2018;**61**:2278−91.
42. Chen Z, Mori W, Deng X, Cheng R, Ogasawara D, Zhang G, et al. Design, synthesis and evaluation of reversible and irreversible

monoacylglycerol lipase positron emission tomography (PET) tracers using a 'tail switching' strategy on a piperazinyl azetidine skeleton. *J Med Chem* 2019;**62**:3336−53.

43. Wang C, Placzek MS, Van de Bittner GC, Schroeder FA, Hooker JM. A novel radiotracer for imaging monoacylglycerol lipase in the brain using positron emission tomography. *ACS Chem Neurosci* 2016;**7**:484−9.
44. Ahamed M, Attili B, van Veghel D, Ooms M, Berben P, Celen S, et al. Synthesis and preclinical evaluation of [^{11}C]MA-PB-1 for *in vivo* imaging of brain monoacylglycerol lipase (MAGL). *Eur J Med Chem* 2017;**136**:104−13.
45. Yamasaki T, Mori W, Zhang Y, Hatori A, Fujinaga M, Wakizaka H, et al. First demonstration of *in vivo* mapping for regional brain monoacylglycerol lipase using PET with [^{11}C]SAR127303. *NeuroImage* 2018;**176**:313−20.
46. Zhang L, Butler CR, Maresca KP, Takano A, Nag S, Jia Z, et al. Identification and development of an irreversible monoacylglycerol lipase (MAGL) positron emission tomography (PET) radioligand with high specificity. *J Med Chem* 2019;**62**:8532−43.
47. Hattori Y, Aoyama K, Maeda J, Arimura N, Takahashi Y, Sasaki M, et al. Design, synthesis, and evaluation of (4*R*)-1-{3-[2-(^{18}F)fluoro-4-methylpyridin-3-yl]phenyl}-4-[4-(1,3-thiazol-2-ylcarbonyl)piperazin-1-yl]pyrrolidin-2-one ([^{18}F]T-401) as a novel positron-emission tomography imaging agent for monoacylglycerol lipase. *J Med Chem* 2019;**62**:2362−75.
48. Chen Z, Mori W, Fu H, Schafroth MA, Hatori A, Shao T, et al. Design, synthesis, and evaluation of ^{18}F-labeled monoacylglycerol lipase inhibitors as novel positron emission tomography probes. *J Med Chem* 2019;**62**:8866−72.
49. Schalk-Hihi C, Schubert C, Alexander R, Bayoumy S, Clemente JC, Deckman I, et al. Crystal structure of a soluble form of human monoglyceride lipase in complex with an inhibitor at 1.35 Å resolution. *Protein Sci* 2011;**20**:670−83.
50. Chen Z, Cheng R, Yang J, Shao T, Vasdev N, Ran C, et al. A novel ^{18}F-labeled MAG lipase biomarker for differentiating brown and white adipose tissue in the lipid network. *J Nucl Med* 2018;**59**:262.
51. OECD. Test No. 107: partition coefficient (n-octanol/water): Shake Flask method. OECD Publishing; 1995. Available from: https://www.oecd-ilibrary.org/environment/test-no-107-partition-coefficient-n-octanol-water-shake-flask-method_9789264069626-en.
52. Waterhouse RN. Determination of lipophilicity and its use as a predictor of blood−brain barrier penetration of molecular imaging agents. *Mol Imaging Biol* 2003;**5**:376−89.
53. Patel S, Gibson R. *In vivo* site-directed radiotracers: a mini-review. *Nucl Med Biol* 2008;**35**:805−15.
54. Pike VW. Considerations in the development of reversibly binding PET radioligands for brain imaging. *Curr Med Chem* 2016;**23**:1818−69.
55. Baell JB, Holloway GA. New substructure filters for removal of pan assay interference compounds (PAINS) from screening libraries and for their exclusion in bioassays. *J Med Chem* 2010;**53**:2719−40.
56. Cravatt BF, Wright AT, Kozarich JW. Activity-based protein profiling: from enzyme chemistry to proteomic chemistry. *Annu Rev Biochem* 2008;**77**:383−414.
57. Besnard J, Ruda GF, Setola V, Abecassis K, Rodriguiz RM, Huang XP, et al. Automated design of ligands to polypharmacological profiles. *Nature* 2012;**492**:215−20.
58. Kroeze WK, Sassano MF, Huang XP, Lansu K, McCorvy JD, Giguère PM, et al. PRESTO-Tango as an open-source resource for interrogation of the druggable human GPCRome. *Nat Struct Mol Biol* 2015;**22**:362−9.
59. Wang L, Yui J, Wang Q, Zhang Y, Mori W, Shimoda Y, et al. Synthesis and preliminary PET imaging studies of a FAAH radiotracer ([^{11}C]MPPO) based on α-ketoheterocyclic scaffold. *ACS Chem Neurosci* 2016;**7**:109−18.
60. Chen Z, Mori W, Zhang X, Yamasaki T, Dunn PJ, Zhang G, et al. Synthesis, pharmacology and preclinical evaluation of ^{11}C-labeled 1,3-dihydro-2*H*-benzo[*d*]imidazole-2-ones for imaging γ8-dependent transmembrane AMPA receptor regulatory protein. *Eur J Med Chem* 2018;**157**:898−908.